The Astrophysical Journal, 853:178 (6pp), 2018 February 1 https://doi.org/10.3847/1538-4357/aaa4f5

Photospheric and Coronal Abundances in an X8.3 Class Limb Flare

G. A. Doschek[1], H. P. Warren[1], L. K. Harra[2], J. L. Culhane[2], T. Watanabe[3], and H. Hara[3]
[1] Space Science Division, Naval Research Laboratory, Washington, DC 20375, USA
[2] UCL-Mullard Space Science Laboratory, Holmbury St. Mary, Dorking, Surrey, RH5 6NT, UK
[3] National Astronomical Observatory, National Institutes of Natural Sciences 2-21-1 Osawa, Mitaka Tokyo, 181-8588, Japan
Received 2017 November 29; accepted 2017 December 28; published 2018 February 5

Abstract

We analyze solar elemental abundances in coronal post-flare loops of an X8.3 flare (SOL2017-09-10T16:06) observed on the west limb on 2017 September 10 near 18 UT using spectra recorded by the Extreme-ultraviolet Imaging Spectrometer (EIS) on the *Hinode* spacecraft. The abundances in the corona can differ from photospheric abundances due to the first ionization potential (FIP) effect. In some loops of this flare, we find that the abundances appear to be coronal at the loop apices or cusps, but steadily transform from coronal to photospheric as the loop footpoint is approached. This result is found from the intensity ratio of a low-FIP ion spectral line (Ca XIV) to a high-FIP ion spectral line (Ar XIV) formed at about the same temperature (4–5 MK). Both lines are observed close in wavelength. Temperature, which could alter the interpretation, does not appear to be a factor based on intensity ratios of Ca XV lines to a Ca XIV line. We discuss the abundance result in terms of the Laming model of the FIP effect, which is explained by the action of the ponderomotive force in magnetohydrodynamic (MHD) waves in coronal loops and in the underlying chromosphere.

Key words: Sun: activity – Sun: corona – Sun: flares – Sun: UV radiation

1. Introduction

On 2017 September 10, the second largest solar flare of this solar cycle, an X8.3 flare, occurred on the west limb in active region 12673. This region emerged and began an extensive development around September 2 on the disk and produced many flares. The X8.3 flare had a rapid rise to maximum X-ray intensity beginning around 16:00 UT and was a long-duration event that ended about 24 hr later. The *Geostationary Operational Environmental Satellite* (*GOES*) X-ray flux is shown in Figure 1.

Many instruments on spacecraft in the suite of the Heliophysics Observatories observed this and other flares in active region 12673 as it traversed the solar disk. The X8.3 flare's limb position offers the opportunity of investigating different features of the Standard Flare Model (e.g., see Figure 1 in Reeves & Forbes 2005) that are best seen on the limb. In particular, the flare was well-observed by the Extreme-ultraviolet Imaging Spectrometer (EIS) on *Hinode* in 15 emission lines, which allows the temperature and density structure of this edge-on loop arcade to be investigated in considerable detail. Raster images of the flare can be constructed in single emission lines, which enables highly accurate temperatures to be determined in different parts of the flare. This paper is one of several EIS papers concerning different aspects of the X8.3 flare.

The focus here is on solar coronal abundances in the X8.3 flare and flares in general. Abundances in the corona and photosphere can be different due to the first ionization potential (FIP) effect. The FIP effect was noted as long ago as 1985 (e.g., Meyer 1985a, 1985b). Those elements with FIPs greater than about 10 eV are believed to have the same composition in the corona as in the photosphere. Elements with FIPs less than about 10 eV have abundances of about three to four times greater in the corona than in the photosphere. The effect is also apparent in the composition of solar energetic particles (SEPs) detected near the Earth. There is extensive observational literature on the subject (e.g., Feldman 1992; Schmelz et al. 2012; Reames 2014). The most sophisticated model of the FIP effect has been developed by Laming (2004, 2015). In the Laming model, the FIP effect is caused by a ponderomotive force generated in waves such as Alfvén waves and can operate to preferentially populate coronal loops with low-FIP elements.

In this paper, we focus on the Ca XIV and Ar XIV lines near 194 Å, a wavelength region well-observed by EIS. The Ar XIV and Ca XIV lines are formed near 4–5 MK. Determining abundances with different line intensity ratios with EIS is described in Feldman et al. (2009), and determining those using the Ca XIV/Ar XIV ratio is discussed in detail in Doschek & Warren (2017). The method depends on finding low-FIP/high-FIP line pairs formed at about the same temperature, with similar contribution functions. Density sensitivity also plays a role. We take all temperature and density atomic data from CHIANTI (Dere et al. 1997; Landi et al. 2013). For the Ca XIV/Ar XIV ratio, we assume the Ca photospheric abundance given by Caffau et al. (2011) and the Ar photospheric abundance given by Lodders (2008). The coronal Ar abundance is taken to be the same as in the photosphere and the coronal Ca abundance is given by Feldman (1992) or Schmelz et al. (2012). We feel that these coronal and photospheric abundances are the best available at the present time. The solar Ar abundance is actually unknown. We feel that the Lodders (2008) abundance is our best estimate.

Recently, some dramatic new results have been found concerning abundance variations in the corona (Doschek et al. 2015; Doschek & Warren 2016, 2017). These results were found from the intensity ratio of the Ca XIV line at 193.87 Å (low FIP) to the nearby Ar XIV line at 194.40 Å (high FIP). Doschek et al. (2015) discovered a strong Inverse FIP (IFIP) effect in the footpoint areas of a coronal flare loop. In the inverse case, low-FIP ions are less abundant in the corona than in the photosphere. Investigation of EIS data sets revealed that an IFIP effect can occur in small areas near sunspots. More recently, Doschek & Warren (2017) found that the abundances over large areas near sunspots can sometimes be photospheric,

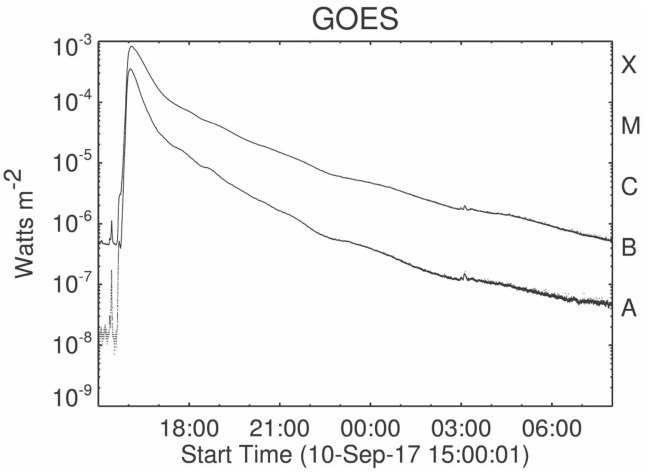

Figure 1. *GOES* X-ray data for the 2017 September 10 X8.3 flare. The upper curve is the 1–8 Å flux; the lower curve is the 0.5–4 Å flux.

or between coronal and photospheric. It is as if the FIP effect can partly shut down near sunspots. This result is consistent with predictions of the Laming model, and is consistent with stellar observations of stars covered with large areas of starspots (e.g., Vogt & Penrod 1983; Drake et al. 2001; Wood et al. 2012; Wood & Laming 2013).

In the Laming model, the IFIP effect occurs when the ponderomotive force points toward the chromosphere instead of into the corona. This occurs when the magnetic fields of loops become very strong. There is a competition between waves that are resonant in the loops and fast mode waves in the chromosphere that are reflected and do not enter the loops. The loop waves when reflected upward back into the loops pull the low-FIP ions with them (the FIP effect). When the fast mode waves are reflected back down to lower levels of the atmosphere they pull the low-FIP ions with them (IFIP effect). In the late-type stars, the stronger fields in the loops and the strong convection favor the dominance of the fast mode waves and the IFIP effect wins over the FIP effect. The low-FIP ions are pushed downward toward lower temperatures in the chromosphere instead of upward into the corona. In the Sun, the reversal of the ponderomotive force is more likely to occur in the strong magnetic field regions of sunspots. Although the above results were found in EIS spectra from the Ar XIV/Ca XIV intensity ratio, the effect is also found for lines of Ar XI, an ion formed at considerably cooler temperatures.

In the hot core loops of active regions, measurements of the Ar XIV/Ca XIV intensity ratio yield a coronal abundance, i.e., calcium is about three to four times more abundant in these loops than in the photosphere. However, in a study of EUV flare spectra from the Extreme-ultraviolet Variability Experiment (EVE) spectrometer on the *Solar Dynamics Observatory* (*SDO*), Del Zanna (2013b) and Warren (2014) concluded that the abundances in flares are photospheric. Warren (2014) used line to continuum ratios to obtain this result. The result seems logical. It is also predicted by the Laming (2015) model. In a flare, plasma is rapidly expelled into coronal loops by chromospheric evaporation and would not have time for an FIP effect to occur. However, Doschek et al. (2015) found in EIS spectra that in the bright regions of flares, the Ar XIV/Ca XIV ratios yielded coronal abundances, an apparent contradiction of the EVE result. The EIS exceptions are the IFIP effects and regions near sunspots mentioned above. But even in these regions the brightest plasma seems to have coronal abundances.

The EVE results depend mostly on spectral lines of flare iron ions. Iron is considered a low-FIP element but its behavior as a low-FIP element has been question by results from the Solar Assembly for X-rays (SAX) on the *MESSENGER* spacecraft (e.g., Dennis et al. 2015). The flare iron lines are mostly hotter than the calcium and argon lines. This could play a role in reconciling the EIS results with the EVE results. The central question is what is the flare composition, coronal or photospheric.

The X8.3 flare has offered some new and perplexing information about abundances in flares. In this paper, we investigate the Ar XIV/Ca XIV ratio in post-flare loops of the X8.3 flare from the loop apex to their footpoints. In some loops, we find a striking transformation from a coronal FIP effect at the loop apex to near photospheric abundances near the footpoints. This result may help resolve the EIS/EVE abundance differences.

The instrument and data reduction are briefly described in Section 2. Spectra and results are given in Section 3, followed by a short discussion in Section 4.

2. THE EIS Spectrometer and Data Reduction

The EIS spectrometer is described by Culhane et al. (2007). EIS observes two narrow wavelength bands between about 170–213 Å and 250–290 Å. A multi-layer coated articulated telescope mirror images the Sun onto one of four slit/slot apertures oriented in the north–south direction. The light passing through a slit/slot is diffracted by a multi-layer coated toroidal grating and imaged onto two CCD detectors. Up to 25 spectral lines can be observed in narrow wavelength windows. Or a full-CCD study can be selected, i.e., the entire wavebands of both CCDs are recorded.

The X8.3 flare was detected using the Flare266_hunter01 study and the *Hinode* X-ray Telescope (XRT) flare trigger. The EIS flare hunter routine uses the widest slot (266″) and observes the 256 Å He II line. After flare detection, the EIS FlareResponse01 study was used. This study observes 15 lines that cover a broad temperature range from O IV up to Fe XXIV.

The EIS data are processed using standard EIS software for dark current, the CCD pedestal, warm pixels, slit tilt, and temperature variations due to the *Hinode* orbit. We have used the old EIS calibration instead of the new calibrations discussed by Del Zanna (2013a) or Warren et al. (2014). The argon and calcium lines are so close in wavelength that this calibration is sufficient.

3. Results

Figure 2 shows images of the flare in a combined Ca and Ar line image and in an Fe XXIV line at two different times. The faint approximately 45° diagonal streaks, most apparent in the top left image, are multiple diffraction images and are not physical. However, the horizontal streak in the Fe XXIV images is the current sheet and is discussed by Warren et al. (2018). In the 18 UT images, the flare has grown in size and is slowly expanding outward from the Sun. The Ca, Ar image was produced by making an image (totaling the intensity) of the entire wavelength window from 193.66 Å to 194.52 Å. This window covers the wavelengths of both the Ar and the Ca lines. By 18:39 UT, there is an extensive post-flare loop

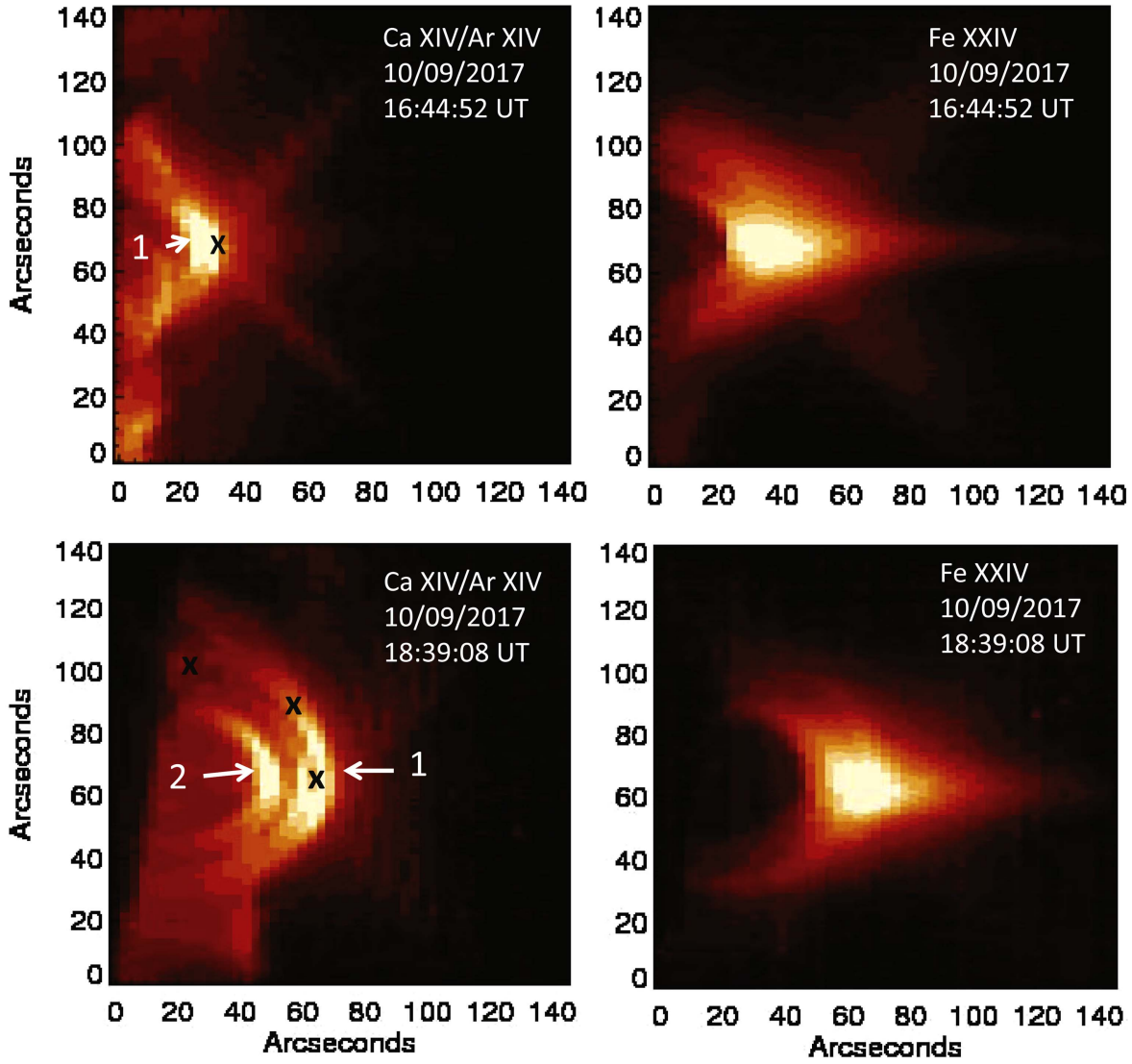

Figure 2. Images of the X8.3 flare in spectral lines of Fe XXIV and combined lines of Ca XIV and Ar XIV. The faint approximately 45° streaks (best seen in the top left panel) are multiple diffraction images and are not physical. The Xs in the lower left panel are positions where the Ca/Ar spectra are plotted in Figure 5. The X in the top left panel is the position of the spectrum in Figure 7. The numbers 1 and 2 refer to loops discussed in the text. The times in the figure are the raster start times.

development. Note that in the images multiple loops are seen along the line of sight, demonstrating that we are observing a loop arcade on edge. An example of a flare loop arcade seen on the disk is well-illustrated by a famous Bastille Day solar storm (see Figures 6, 7, and 8 in Aschwanden & Alexander 2001). The development of the X8.3 flare in time from a relatively small and extremely bright region into large developed loops over increasing spatial scales is typical for long-duration events and was well-observed by the Solar X-Ray Telescope (SXT) on *Yohkoh* (e.g., Feldman et al. 1995) and is frequently seen in data from the X-ray telescope (XRT) on *Hinode* and the Atmospheric Imaging Assembly (AIA) extreme-ultraviolet (EUV) imaging telescopes on *SDO*.

Inspection of the Fe and Ca images in Figure 2 shows that the hottest region of the flare was the cusp region, as it is extended in the hot ion Fe XXIV images but only very marginally in the Ca XIV images. The temperature in the cusp is discussed by Warren et al. (2018); it is at least 10 MK based on ionization equilibrium calculations for Fe XXIV. Intensity line ratios of Ca XV/Ca XIV and Fe XVI/Fe XV also show slight temperature increases right above the brightest portions of the flare loops, supporting the higher temperature in the cusp. However, the Ca and Ar images represent plasma with temperatures of about 4.5 MK, according to ionization equilibrium calculations. Regardless of temperature, the high electron densities in flares should result over time in only small non-ionization equilibrium effects except for an ion like Fe XXVI, where ionization from Fe XXV requires removal of a K-shell electron.

Large flares are usually accompanied by filament eruptions that signal the onset of a flare. The filament plasma is considerably cooler than the Fe XXIV plasma. In Figure 3, we show two small (marked in the figure) emission features in the corona (obtained earlier than the images in Figure 2) above the flare cusp. Images in Fe XI and Fe XII (about 1.4 MK) show large Doppler line-of-sight speeds, which vary within the small regions. Region 1 is approaching us along the line of sight by about 200–400 km s^{-1}. Region 2 is receding from us at about the same speed. These small plasma regions are probably part of the filament.

A logarithmic image of the Ca XIV/Ar XIV ratio is shown in Figure 4 for the later time 18:39:08 UT. Clearly the ratio is

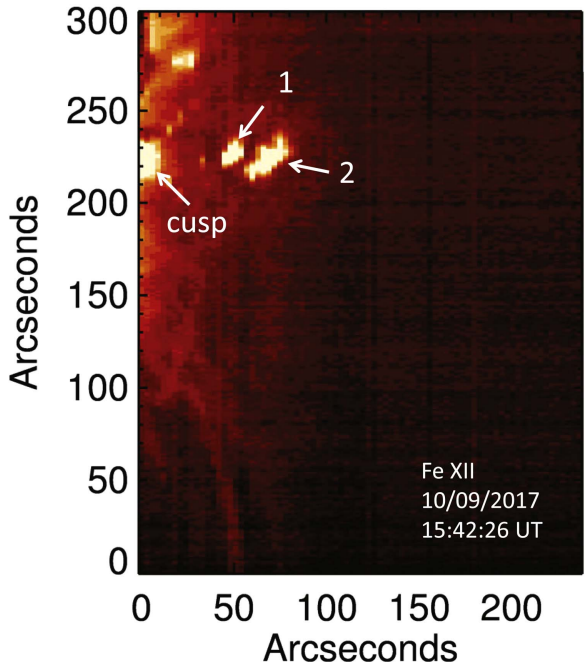

Figure 3. Pieces of the plasma filament seen in an emission line of Fe XII near the beginning of the flare. The two pieces above the cusp are approaching (1) and receding from us (2). The approaching and receding speeds are 200–400 km s^{-1}.

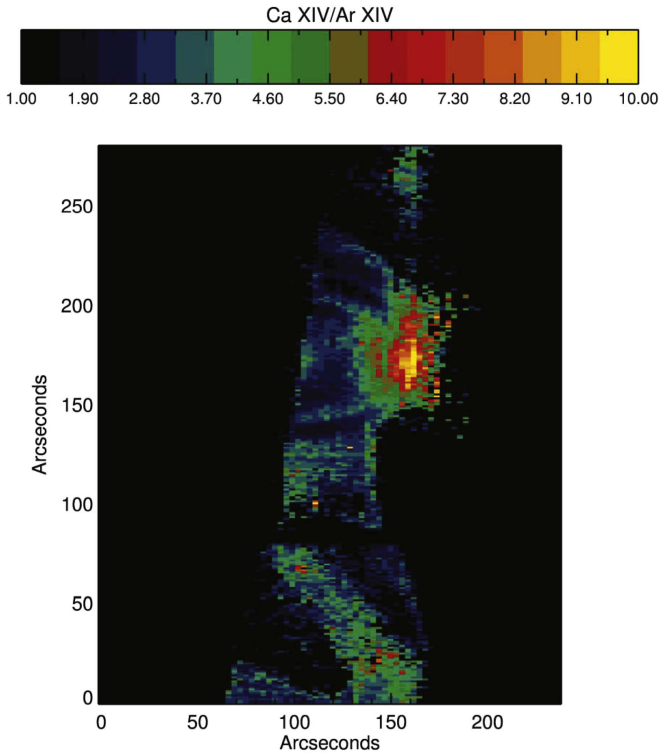

Figure 4. Ca XIV/Ar XIV ratio. This ratio is an indicator of abundance. A large ratio (about 10) indicates a coronal abundance. A small ratio (about 1–1.9) indicates a photospheric abundance. Note also that the diffraction is faintly visible.

largest at the loop tops of the flare and becomes less along the loop legs. The diagonal diffraction images are faintly present in this figure.

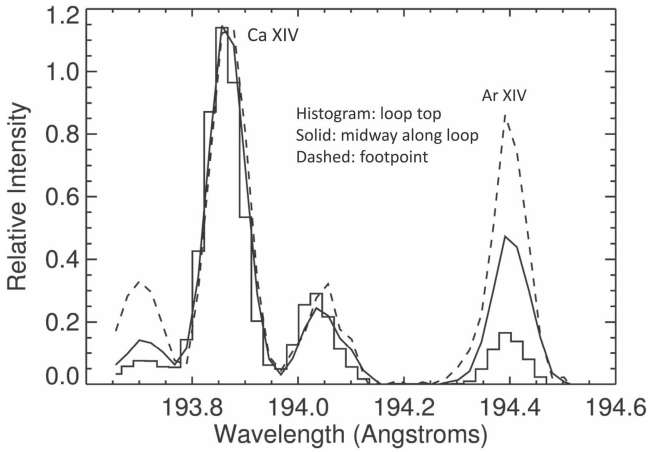

Figure 5. Ca and Ar spectra for three positions in loop 1 marked by an X in Figure 2. A Ca XIV/Ar XIV ratio of about 4 or more implies coronal abundances. A ratio of about 0.6–1 implies photospheric abundances. The line near 193.7 Å is a line of Fe X.

The change in line ratio along the loop lengths is best illustrated by the spectra along the leg. Figure 5 shows three spectra at the locations marked by "*X*" in Figure 2 (lower left panel). The histogram spectrum is the spectrum in the center of the cusp. It exhibits coronal abundances because the Ca XIV line intensity is about four or more times greater than the Ar XIV line intensity. If the lines had comparable intensities, the abundances would be photospheric. Note that in the positions along the legs away from the cusp that the Ar XIV intensity increases relative to the Ca XIV line intensity. The change is quite large. In the *X* nearest the footpoint, the abundances are about photospheric. The spectra for the three positions were made by averaging the spectra at the x, y position with the pixels at x–1, x+1 and y–1, y+1. The same effect is also noted in the main Ca/Ar loop at 16:44:52 UT, so this is not a temporary transient effect.

The ratio of the Ca XIV and Ar XIV lines is sensitive to both temperature and density (see Figure 1 in Doschek & Warren 2017). The Ar XIV/Ca XIV ratio increases greatly if the temperature becomes really large, beyond the temperature at which the Ca and Ar lines are formed in ionization equilibrium. This would mimic a progression from coronal to photospheric if the temperature increased greatly along the loop from the cusp to the footpoint. Therefore we examined the intensity ratio of two lines of Ca XV (181.91 Å and 200.972 Å) to the intensity of the Ca XIV line we are discussing (193.86 Å). If this ratio increases substantially, it would imply an increase of temperature.

In Figure 6, we show the Ar XIV/Ca XIV ratio and the ratio of the Ca XV lines to the Ca XIV line. It is clear from this figure that the increased intensity of the Ar line is not caused by temperature. From CHIANTI, a Ca XV/Ca XIV ratio of 1.2 corresponds to a temperature of about 5.4 MK. If the ratio increases to say 1.4, the temperature increases to 5.8 MK, but in this temperature range the Ar/Ca ratio is at its minimum and does not start a significant increase until the temperature starts rising above 5.8 MK (see Figure 1 in Doschek & Warren 2017).

Note also in Figure 5 that the centroid of the blended feature near 194.05 Å moves slightly to the red as the Ar XIV line increases in intensity. That is because an Ar XI line falls at 194.09 Å and is badly blended with a Ni XVI line at 194.04 Å.

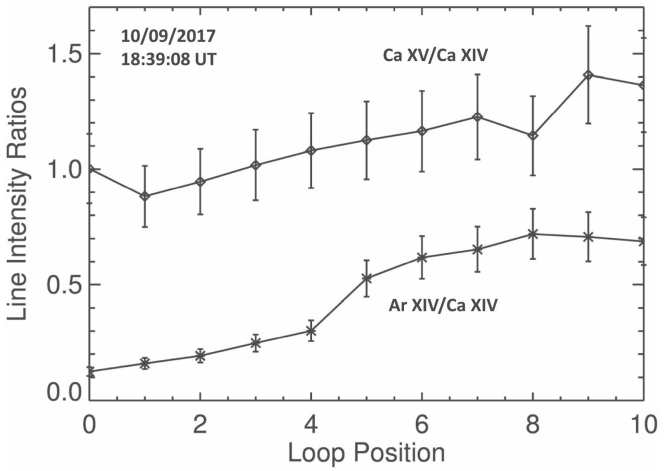

Figure 6. Indicated line ratios at various positions along loop 1 in Figure 2 beginning at the cusp (position 0) and proceding toward the footpoint. The error bars are statistical uncertainties. Loop 1 is an approximately circular loop seen in projection with a radius of about 3×10^3 km s^{-1}.

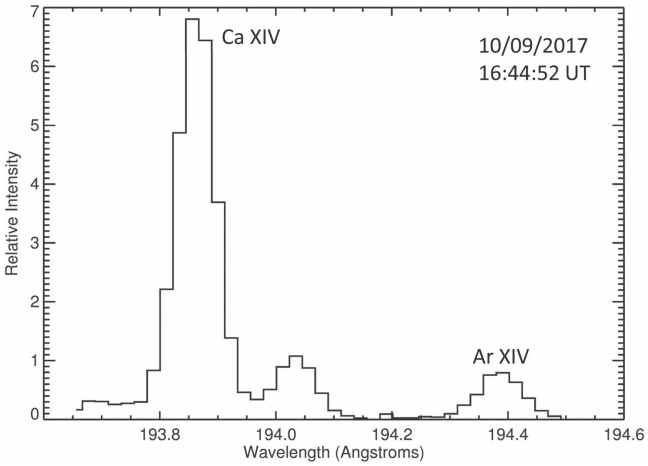

Figure 7. Spectrum at the X location in the 16:44:52 UT image of Ca/Ar in Figure 2.

The increase in Ar intensities with different ionization stages is consistent with an abundance interpretation.

The effect of density cannot cause the large Ar/Ca ratios. However, we have measured densities in the loops under discussion. The intensity ratio, Ca XV(181.91 Å)/Ca XV (200.972 Å) is density sensitive. At log densities of 8 and 9, the 182 Å line is very weak and too weak to observe with EIS. But at densities between 10 and 12 the ratio increases up to a value of about 2.43 at a density of 12. We have measured this ratio along loop 1 in Figure 2 but find that near the footpoints the 182 Å intensity is really too unreliable to give meaningful densities. But inside the cusp the ratio is usable.

In the 16:44:52 Ca/Ar cusp region marked by the X, we find a density of 4.8×10^{10} cm^{-3}. In the center of the 16:44:52 UT cusp, where the Ca XIV line is saturated, the density is higher, around 5.8×10^{10} cm^{-3} The density in the center of this cusp is a bit higher than elsewhere in the loop. The density is nearly constant in much of the loop but decreases somewhat toward the footpoints. In the 18:39:08 UT cusp, the density is about 2×10^{10} cm^{-3} and the Ar/Ca ratio is around 0.11. In the earliest spectra of this flare, loop structures cannot be resolved. There is simply a bright blob-like feature.

An interesting result is that the Ar/Ca ratio in the cusp (0.11) is smaller than usual for a coronal abundance. This is illustrated in Figure 7, where the spectrum is shown at the X in the 16:44:52 UT Ca/Ar image in Figure 2. The Ar XIV/Ca XIV ratio is 0.12 at the tip of the cusp right before entering the current sheet. Right at the center of the cusp, the Ca XIV line is saturated and the ratio is probably even smaller. A ratio of 0.12 is about 1/2 the ratio in a typical coronal abundance, implying a kind of super coronal abundance. However, we feel that this low value is mainly an effect of temperature. Inspection of Figure 1 in Doschek & Warren (2017) shows that the Ar/Ca ratio reaches its lowest value (both photospheric and coronal) near a temperature of 5 MK. This is near the temperature we obtain from the Ca XV/Ca XIV ratio mentioned above.

So far we have discussed mainly one leg of loop 1 in Figure 2. What about the other leg? Although it is difficult to see in the Figure 2 reproduction, the southern leg of loop 1 is actually two legs (and probably more). The outermost leg shows a good Ar/Ca enhancement toward photospheric abundances. However, the inner leg shows a small enhancement, but not much. These loops are seen nearly along the same line of sight, but they could be considerably separated spatially from one another in the flare arcade.

The result for loop 2 in Figure 2 is similar to loop 1 but not quite as pronounced. The take-away from our results is that the flare loop abundances change along some of the loops, proceding from coronal abundances at the loop tops toward photospheric abundances at the footpoints. Also, the rather high electron temperature near 5 MK implies that the Ar/Ca ratio can reach photospheric abundances at a value less than 1 and also cause the appearance of an extreme coronal abundance in the loop cusp region.

4. Discussion

To summarize the results, the Ca XIV and Ar XIV temperature is about 5.4 MK in this flare. At these temperatures and densities, we obtain from two lines of Ca XV, Figure 1 in Doschek & Warren (2017) shows that the coronal Ar XIV/Ca XIV intensity ratio should be less than 0.25, closer to about 0.1, and this is observed. The photospheric abundance ratio should be less than 1, around 0.5–0.6.

The post-flare loops we see are probably several loops from an arcade. Within each loop are probably unresolved strands at different temperatures. For example, Fe XXIV and Fe XXIII emission is also seen at the Xs in Figure 2, but their temperatures are so high that it is hard to imagine all the iron, calcium, and argon emission coming from the same magnetic strands that produce Fe XXIII and Fe XXIV. Another curious result is that the 16:44:52 UT loop does not appear to be in pressure equilibrium, i.e., the pressure is highest in the cusp. And what is causing the abundances to vary in the loops?

One explanation is that the plasma in the loop top regions is a blend of loops along the line of sight that have been in the corona long enough for the abundances to become coronal. The emission we see along the loop toward the footpoint represents loops or strands of loops that have not been in the corona as long as the loop top regions, and this plasma tends toward photospheric abundances. In other words, what looks like a single loop in the images is a blend of loops or a blend of magnetic strands within loops along the line of sight in a large loop arcade. This would cause apparent variability of

abundances along the blended loop structures. However, we note that in the earliest spectra around 15:50 UT the Ar/Ca intensity ratio is coronal (around 0.11) everywhere. But loop structures cannot be resolved. The observed blob-like emission at the earliest observation times is probably a thoroughly mixed collection of loops along the line of sight.

The above results suggest that we still have much to learn about the behavior of ions under the explosive conditions of solar flares.

Hinode is a Japanese mission developed and launched by ISAS/JAXA, collaborating with NAOJ as a domestic partner, and NASA (USA) and STFC (UK) as international partners. Scientific operation of the *Hinode* mission is conducted by the *Hinode* science team organized at ISAS/JAXA. This team mainly consists of scientists from institutes in the partner countries. Support for the post-launch operation is provided by JAXA and NAOJ, STFC, NASA, ESA (European Space Agency), and NSC (Norwegian Space Center). We are grateful to the *Hinode* team for all their efforts in the design, build, and operation of the mission.

G.A.D. and H.P.W. acknowledge support from the NASA *Hinode* program. We thank Dr. Martin Laming for helpful comments on the manuscript.

ORCID iDs

G. A. Doschek https://orcid.org/0000-0002-7625-9866
H. P. Warren https://orcid.org/0000-0001-6102-6851

References

Aschwanden, M. J., & Alexander, D. 2001, SoPh, 204, 91
Caffau, E., Ludwig, H.-G., Steffen, M., Freytag, B., & Bonifacio, P. 2011, SoPh, 268, 255
Culhane, J. L., Harra, L. K., James, A. M., et al. 2007, SoPh, 243, 19
Del Zanna, G. 2013a, A&A, 555, A47
Del Zanna, G. 2013b, A&A, 558, A73
Dennis, B. R., Phillips, K. J. H., Schwartz, R. A., et al. 2015, ApJ, 803, 67
Dere, K. P., Landi, E., Mason, H. E., Monsignori Fossi, B. C., & Young, P. R. 1997, A&AS, 125, 149
Doschek, G. A., & Warren, H. P. 2016, ApJ, 825, 36
Doschek, G. A., & Warren, H. P. 2017, ApJ, 844, 52
Doschek, G. A., Warren, H. P., & Feldman, U. 2015, ApJL, 808, L7
Drake, J. J., Brickhouse, N. S., Kashyap, V., et al. 2001, ApJL, 548, L81
Feldman, U. 1992, PhyS, 46, 202
Feldman, U., Seely, J. F., Doschek, G. A., et al. 1995, ApJ, 446, 860
Feldman, U., Warren, H. P., Brown, C. M., & Doschek, G. A. 2009, ApJ, 695, 36
Laming, J. M. 2004, ApJ, 614, 1063
Laming, J. M. 2015, LRSP, 12, 2
Landi, E., Young, P. R., Dere, K. P., Del Zanna, G., & Mason, H. E. 2013, ApJ, 763, 86
Lodders, K. 2008, ApJ, 674, 607
Meyer, J.-P. 1985a, ApJS, 57, 173
Meyer, J.-P. 1985b, ApJS, 57, 151
Reames, D. V. 2014, SoPh, 289, 977
Reeves, K. K., & Forbes, T. G. 2005, ApJ, 630, 1133
Schmelz, J. T., Reames, D. V., von Steiger, R., & Basu, S. 2012, ApJ, 755, 33
Vogt, S. S., & Penrod, G. D. 1983, PASP, 95, 565
Warren, H. P. 2014, ApJL, 786, L2
Warren, H. P., Brooks, D. H., Ugarte-Urra, I., et al. 2018, ApJ, in press
Warren, H. P., Ugarte-Urra, I., & Landi, E. 2014, ApJS, 213, 11
Wood, B. E., & Laming, J. M. 2013, ApJ, 768, 122
Wood, B. E., Laming, J. M., & Karovska, M. 2012, ApJ, 753, 76